

pubs.acs.org/ac Article

# Frequency-Domain Low-Wavenumber Hyperspectral Stimulated Raman Scattering Microscopy

Matthew G. Clark, Karsten J. Mohn, Bin Dong, Helen C. Campbell, and Chi Zhang\*



Cite This: Anal. Chem. 2024, 96, 10341–10347



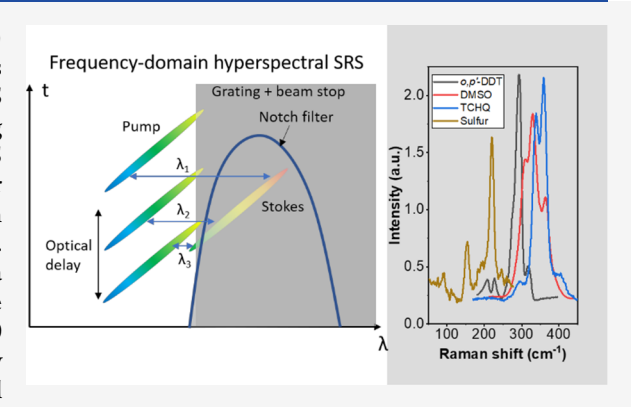
**ACCESS** 

III Metrics & More

Article Recommendations

s Supporting Information

ABSTRACT: In recent years, stimulated Raman scattering (SRS) microscopy has experienced rapid technological advancements and has found widespread applications in chemical analysis. Hyperspectral SRS (hSRS) microscopy further enhances the chemical selectivity in imaging by providing a Raman spectrum for each pixel. Time-domain hSRS techniques often require interferometry and ultrashort femtosecond laser pulses. They are especially suited to measuring low-wavenumber Raman transitions but are susceptible to scattering-induced distortions. Frequency-domain hSRS microscopy, on the other hand, offers a simpler optical configuration and demonstrates high tolerance to sample scattering but typically operates within the spectral range of 400–4000 cm<sup>-1</sup>. Conventional frequency-domain hSRS microscopy is widely employed in biological applications but falls short in detecting chemical bonds with a weaker vibrational energy. In this work, we extend the



spectral coverage of picosecond spectral-focusing hSRS microscopy to below 100 cm<sup>-1</sup>. This frequency-domain low-wavenumber hSRS approach can measure the weaker vibrational energy from the sample and has a strong tolerance to sample scattering. By expanding spectral coverage to 100–4000 cm<sup>-1</sup>, this development enhances the capability of spectral-domain SRS microscopy for chemical imaging.

# INTRODUCTION

Compared to spontaneous Raman scattering, coherent Raman scattering processes, such as stimulated Raman scattering (SRS) and coherent-anti-Stokes Raman scattering (CARS), offer significantly stronger signal levels and faster speed for chemical imaging. <sup>1–6</sup> Both SRS and CARS utilize synchronized pump and Stokes laser pulses to excite the vibrational transitions of molecules. <sup>7–11</sup> Unlike CARS, SRS signals maintain the Lorentzian Raman spectral line shape and have a linear dependence on molecular concentrations, making it a preferred technology among biologists and chemists. <sup>9,12</sup> To enhance chemical contrasts, hyperspectral SRS (hSRS) imaging methods have been developed. <sup>13–15</sup> Typically, two primary approaches are employed to achieve hSRS, depending on whether the spectrum is acquired in the time domain or frequency domain.

Time-domain hSRS usually involves the use of femtosecond laser pulses with ultrashort pulse duration to excite Raman transitions via impulsive SRS processes, which modulate the probe laser pulse to generate an interferogram. <sup>16,17</sup> Subsequent Fourier transform of the interferogram allows for extraction of the frequency-domain Raman spectrum. The spectral coverage is determined by the pulse's frequency breadth, while the spectral resolution is inversely proportional to the acquisition time delay of the interferogram. This method is particularly suitable for measuring low-wavenumber Raman transi-

tions. 18,19 However, the reliance on interferometry renders time-domain measurements vulnerable to sample scattering. Moreover, simultaneous coverage of both low and higher wavenumbers necessitates very short laser pulses, often requiring ultrabroadband lasers and complex pulse precompensation.

Frequency-domain hSRS techniques typically employ widely used dual-output high-repetition-rate femtosecond or picosecond laser systems emitting pulses in the near-IR range with high energy. SRS spectra can be obtained through several methods: adjusting the frequency of one of the two narrowband excitation pulses, sweeping the time delay between two chirped broadband pulses for spectral focusing, or employing both a narrowband pulse and a broadband pulse simultaneously through parallel spectral detection. <sup>13–15,20–24</sup> Due to its straightforward implementation and high tolerance to sample scattering, frequency-domain hSRS is extensively applied in biochemical imaging. However, current frequency-

Received: March 9, 2024 Revised: May 27, 2024 Accepted: June 4, 2024 Published: June 12, 2024





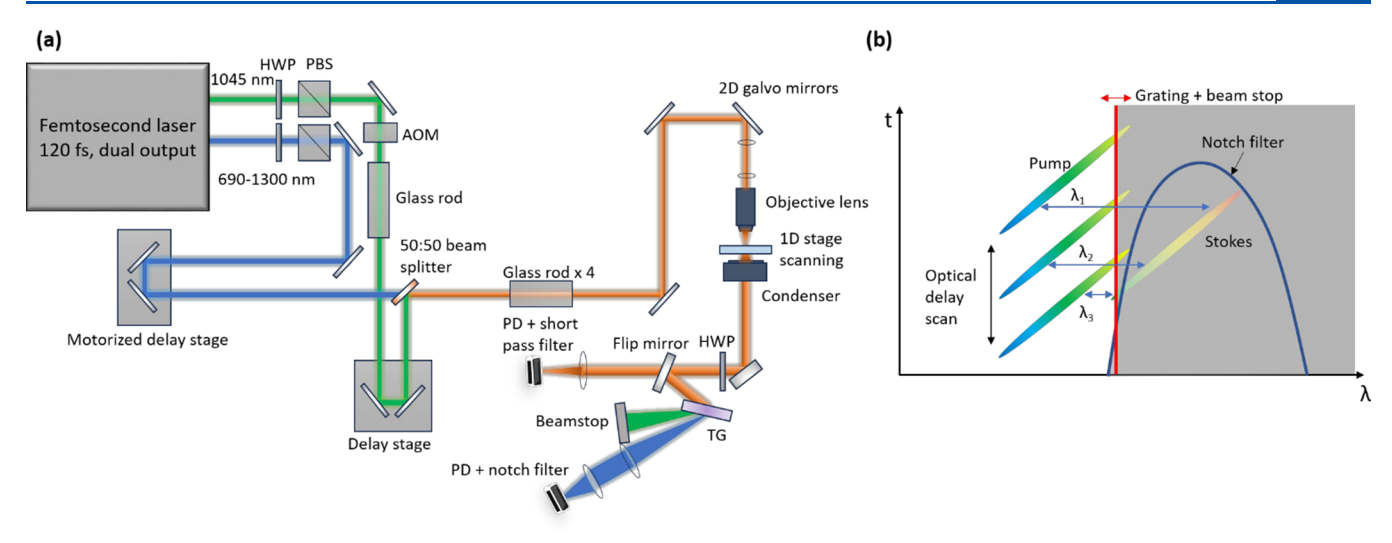


**Figure 1.** Picosecond hSRS for the detection of Raman transitions between 100 and 4000 cm<sup>-1</sup>. (a) Schematic of the hSRS microscope. For detecting Raman transitions above 634 cm<sup>-1</sup>, two-dimensional laser scanning and a photodiode with a short-pass filter are employed. For the detection of Raman transitions below 634 cm<sup>-1</sup>, a one-dimensional laser scanning plus transmission grating configuration is utilized. HWP, half-wave plate; PBS, polarizing beam splitter cube; AOM, acousto-optic modulator; TG, transmission grating; and PD, photodiode. (b) Illustration demonstrates spectral focusing and Stokes beam rejection in the low-wavenumber detection scheme.

domain SRS imaging techniques cover spectral regions including the C–H/O–H region  $(2800-3700~\text{cm}^{-1})$ ,  $^{25-28}$  the silent region  $(1800-2800~\text{cm}^{-1})$ ,  $^{29-34}$  and the fingerprint region  $(400-1800~\text{cm}^{-1})$ ,  $^{26,35-40}$  while neglecting the low-wavenumber region sub-400 cm<sup>-1</sup>. This overlooked spectral region contains rich Raman signatures from chemical bonds with weaker vibrational transitions.

Here, we report a frequency-domain hSRS microscopy technique capable of detecting vibrational Raman transitions below 400 cm<sup>-1</sup>. Leveraging a conventional spectral-focusing hSRS microscopy setup, we broadened the spectral coverage from 100 to 4000 cm<sup>-1</sup>. Encompassing the low-wavenumber region allows the microscope to detect chemicals previously beyond the reach of conventional frequency-domain SRS microscopy. This advancement renders frequency-domain SRS a more comprehensive tool for chemical analysis and imaging.

# **■ EXPERIMENTAL SECTION**

Chemical and Materials. Solid and liquid samples for hSRS imaging were prepared by sandwiching a small amount of sample between two thin glass coverslips with double-sided tape serving as the spacer. 41 A small drop of pure dimethyl sulfoxide (DMSO) or chloroform was sandwiched between the glass coverslips for spectral resolution measurements. A mixed sample of DMSO and chloroform, prepared via serial dilution to the desired ratio, was used to measure the concentration dependence of the SRS signal. Solid samples of 1,1,1-trichloro-2-(o-chlorophenyl)-2-(p-chlorophenyl)ethane (o,p'-DDT, Cayman Chemical, Item No. 24242) and tetrachlorohydroquinone (TCHQ, Cayman Chemical, Item No. 23231) were prepared by dissolving powders in chloroform, followed by deposition and precipitation onto a glass slide. A solid sulfur (Sigma-Aldrich, Item No. 215236) sample was prepared by depositing a small amount of powder onto a glass slide, heating until the sulfur melted to form a  $\sim$ 70  $\mu$ m thin film, and then prepared as previously described for spectroscopy and imaging.

Frequency-Domain Low-Wavenumber SRS System. Details of the conventional frequency-domain hSRS microscope based on spectral focusing can be found in previous

publications. $^{41-43}$  Modifications of the system to achieve low-wavenumber SRS detection are discussed in the Results and Discussion. To facilitate two-dimensional imaging in the low-wavenumber region, a translational stage (H101 and ProScan III, Prior Scientific) is used to enable one-dimensional sample scanning together with one-dimensional galvo mirror scanning. The optical delay stage tuning is achieved by a one-dimensional translation stage (X-LSM050A, Zaber Technologies) at 10  $\mu$ m per step.

SRS signal detection is achieved by using a photodiode (S3994, Hamamatsu) with a resonant circuit centered at 2.4 MHz. The modulation of the Stokes beam is achieved by using an acousto-optic modulator (AOM, M1205-P80L-1, Isomet) commanded by a digital function generator (DG1022Z, Rigol). A digital lock-in amplifier (HF2LI, 50 MHz, Zurich Instruments) is applied for SRS signal extraction. To detect wavenumbers above 200 cm<sup>-1</sup>, the R channel from the lock-in amplifier is utilized. Conversely, for detecting sulfur Raman transitions below 200 cm<sup>-1</sup>, the X channel with a 180° phase shift is employed. The spectra of pump and Stokes pulses, as shown in Figure S1, are measured using an AvaSpec-Mini spectrometer (Avantes USA).

Confocal Spontaneous Raman Scattering Microspectroscopy. A lab-built confocal spontaneous Raman microspectrometer is integrated with the SRS microscope. Raman signal excitation is achieved using a 532 nm single-longitudinal mode laser (CNI laser) with a maximum output of 200 mW. The 532 nm laser is combined with the pump and Stokes laser pulses by a dichroic beam splitter. The spontaneous Raman spectral acquisition is facilitated by a Kymera 328i spectrometer paired with a Newton CCD (1024 × 200 pixels, Oxford Instruments). The CCD was cooled to -80 °C to reduce the thermal noise for spectral acquisition. A notch filter is placed before the spectrometer entrance slit, effectively blocking the 532 nm excitation laser. Signal dispersion is accomplished using a 600 lines/mm grating within the spectrometer. Raman signals from the chemicals are acquired in 2 s, with laser power on the sample set at 100 mW. The

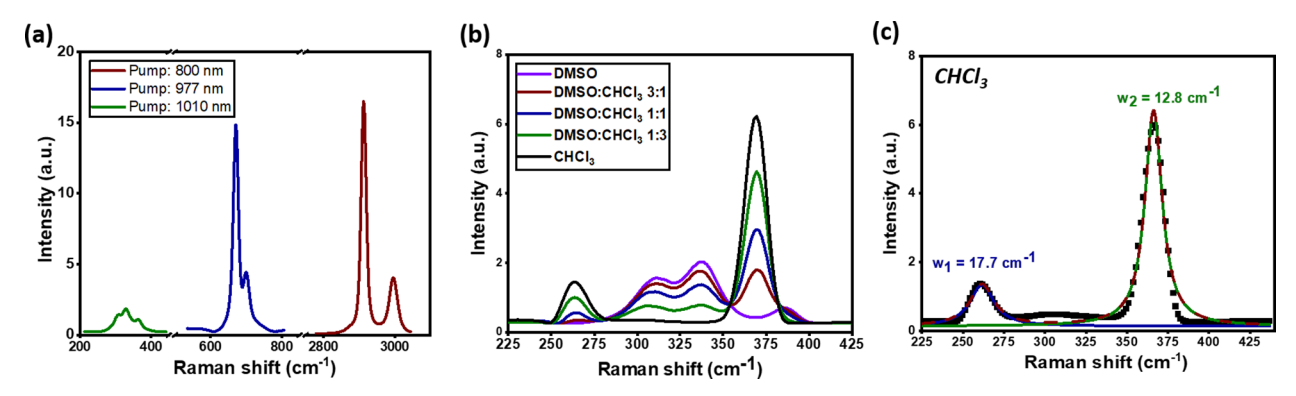


Figure 2. hSRS imaging of liquid samples. (a) SRS spectra of pure DMSO collected in three distinct spectral windows: C-H stretching, fingerprint, and low-wavenumber regions. (b) SRS spectra of CHCl<sub>3</sub> and DMSO mixtures at varying mixing ratios. (c) Spectral fitting for CHCl<sub>3</sub> peaks in the 200–400 cm<sup>-1</sup> range.

acquisition process is managed through Solis software (Oxford Instruments).

Image Acquisition and Analysis. SRS signals are captured using a data acquisition card (PCIe-6363, National Instruments) and lab-written LabVIEW software. The SRS signals are reconstructed by software to form images. The images are saved in TXT format and subsequently processed using ImageJ, where adjustments to contrast and brightness are made for optimal display. Hyperspectral SRS data are converted to image stacks by using ImageJ basic functions. The SRS spectra are processed using Origin 2020 for display and spectral fitting. Lorentzian functions are used for fitting Raman spectra, while Gaussian functions are applied for fitting laser spectra. Standard chemicals such as DMSO are employed to calibrate the Raman shifts obtained in hSRS. Synchronized galvo and sample scanning are conducted through the lab-written LabVIEW software.

# RESULTS AND DISCUSSION

Design of the Frequency-Domain Low-Wavenumber **SRS Microscope.** The optical setup of the low-wavenumber SRS microscope is illustrated in Figure 1a. It employs a synchronized two-color 80 MHz femtosecond laser (InSight X3+, Spectral Physics), with a fixed output at 1045 nm (used as Stokes) and a tunable output from 690 to 1300 nm (used as pump), for SRS excitation. The pump and Stokes laser beams are combined collinearly using a 50/50 beam splitter. The 150 fs pump and Stokes laser pulses are chirped using SF-57 glass rods to 3.4 and 1.8 ps, respectively. 41,42 To enable the detection of the stimulated Raman loss of the pump pulses, the Stokes pulses are modulated at 2.4 MHz by an AOM. The combined laser pulses are directed to a two-dimensional galvano scanning system for imaging. A 60X water dipping objective lens (UPlanSApo 60X/1.2 W, Olympus) focused the laser pulses onto the sample. For measuring Raman transitions above 634 cm<sup>-1</sup>, the laser beams are two-dimensionally rasterscanned by the galvo mirrors and directed to a photodiode equipped with a 980 nm short-pass filter (Chroma Technology). This filter was implemented to selectively reject the Stokes beam, while allowing the pump beam to be detected. This configuration is identical to that of conventional spectral-focusing hyperspectral SRS microscopes, which cannot detect Raman transitions below 634 cm<sup>-1</sup>. The cutoff wavelength of the short-pass filter sets this limit.

A secondary beam path is built to extend the spectral coverage of the hSRS microscope. As illustrated in Figure 1a, a

flip mirror is employed to direct the transmitted pump and Stokes pulses to a transmission grating (1800 lines/mm, LightSmyth, Coherent Corp.) for beam separation. To optimize the diffracting efficiency of the grating, a half-wave plate is positioned before the transmission grating. The diffracted Stokes beam is blocked by a beam stop, while the diffracted pump beam goes through two lenses before reaching a photodiode. Despite the spatial separation of the pump and Stokes pulses, scattering of the Stokes beam by the sample can lead to a strong background (Figure S2). To mitigate this, a 1064 nm notch filter (Edmund Optics, #86-128) with a cutoff frequency near 1030 nm was applied to further attenuate leakage of the Stokes beam into the photodiode (Figure S2a,b). The cutoff frequency of this filter can be fine-tuned by adjusting the angle of the filter relative to that of the incident beam. Using this filter in the conventional hSRS configuration without the implementation of the transmission grating also results in a strong background from Stokes leakage, as shown in Figure S2c. Both spatially separating the pump and Stokes beams using the grating and employing the notch filter are necessary for hSRS microscopy in the low-wavenumber region. The beam stop yields only a modest 10-20% improvement in the background reduction. While this improvement may not be substantial, it is advisable to incorporate the beam stop in the optical path. The application of the grating only allows 1D galvo scanning along the direction of the grating grooves. To achieve two-dimensional imaging, one-dimensional sample stage scanning perpendicular to the one-dimensional galvo scanning is employed for image acquisition.

Figure 1b illustrates the passband characteristics of the filter and the beam stop along with the laser frequencies depicted in the time-wavelength domain. The spatial separation of the pump and Stokes pulses enables effective suppression of the Stokes beam while facilitating the detection of most of the pump beam. The notch filter additionally diminishes leakage of the Stokes beam resulting from inadequate blocking and sample scattering. Tuning the wavelength of the pump beam to approximate that of the Stokes beam allows for the detection of low-wavenumber Raman transitions. Adjustment of the time delay between the chirped pump and Stokes pulses enables hSRS measurements using the spectral focusing methodology. In our current configuration, the pixel dwell time is 10  $\mu$ s, and the imaging speed is 1-2 s per frame, depending on the pixel numbers of each image. A hyperspectral image covering a 200 cm $^{-1}$  spectral window and 100 frames takes  $\sim$ 3 min to collect. The speed of collection is limited by the signal-to-noise-ratio

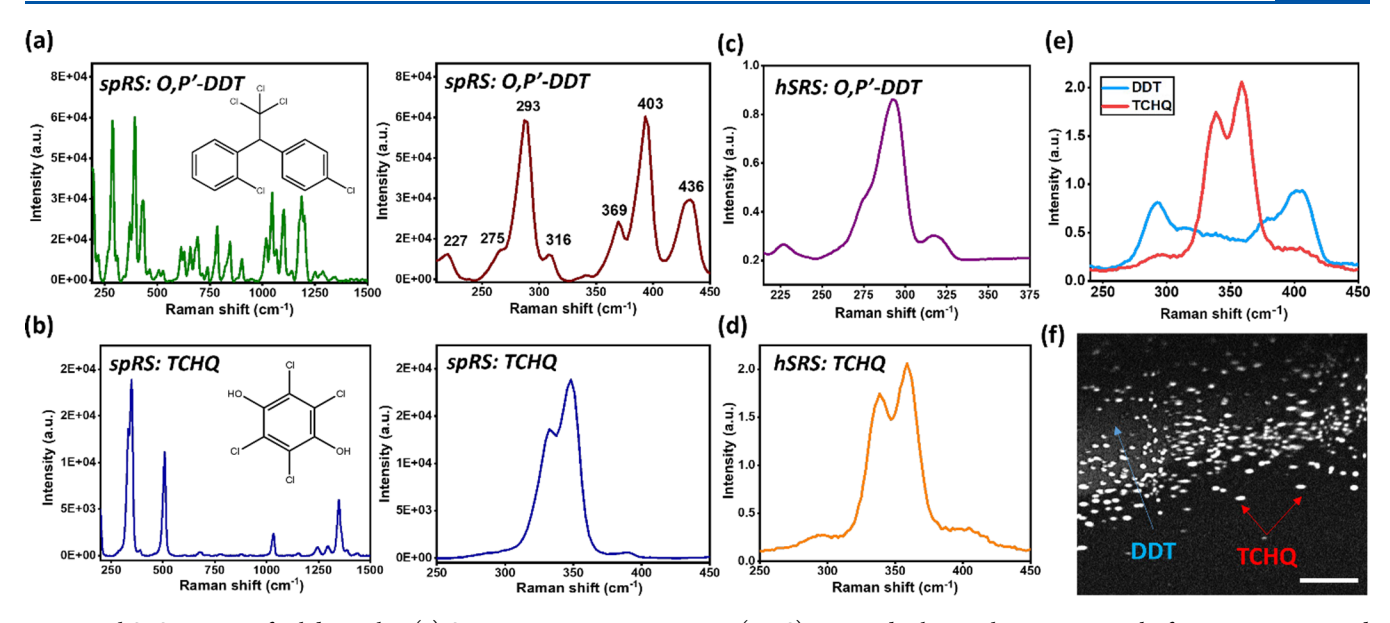


Figure 3. hSRS imaging of solid samples. (a) Spontaneous Raman scattering (spRS) spectra displaying characteristic peaks from 200 to 1500 and 200–450 cm<sup>-1</sup> of o,p'-DDT. (b) spRS spectra displaying characteristic peaks from 200 to 1500 and 250–450 cm<sup>-1</sup> of TCHQ. (c) hSRS spectrum of o,p'-DDT spanning 200–375 cm<sup>-1</sup>. (d) hSRS spectra of TCHQ spanning the range of 250–450 cm<sup>-1</sup>. (e) hSRS spectra of o,p'-DDT and TCHQ within the same spectral range from the mixture sample. (f) SRS image acquired at 360 cm<sup>-1</sup> for a solid mixture of o,p'-DDT and TCHQ drop-casted on a glass slide. Scale bar: 20 μm.

(SNR) from the sample, the pixel dwell time, and ultimately the maximum scanning speed of the galvo mirrors.

Measuring Liquid and Solid Samples Using the Low-Wavenumber Raman Transitions. Extending the hSRS spectral range to low wavenumbers enables the detection of additional Raman transitions that are typically beyond the reach of conventional frequency-domain hSRS. For example, by tuning the pump wavelength to 1010 nm, our system can capture three signature peaks of DMSO in the 200-400 cm<sup>-1</sup> range (Figure 2a). These three peaks, located approximately at  $\sim$ 308, 335, and 384 cm<sup>-1</sup>, correspond to the C-S-C bending, C-S-O out-of-plane bending, and C-S-O in-plane rocking modes, respectively.<sup>44</sup> Adjusting the pump wavelengths to 977 and 800 nm allows us to obtain the SRS spectrum of DMSO spanning the fingerprint region and the C-H stretching region. In the fingerprint region, the two peaks represent symmetric (670 cm<sup>-1</sup>) and asymmetric (700 cm<sup>-1</sup>) stretching of C-S, while in the C-H region, the peaks denote symmetric (2913 cm<sup>-1</sup>) and asymmetric (2997 cm<sup>-1</sup>) stretching of C-H bond in the methyl group. 44 This measurement demonstrates that using the low-wavenumber SRS microscope, we can scan a spectral range that covers all vibrational Raman transitions of DMSO.

Next, we prepared mixtures of DMSO with chloroform at various ratios and obtained the SRS spectra. The pump beam is set to 1013 nm for SRS excitation. The laser power on the sample is 24 mW for the pump pulses and 19 mW for the Stokes pulses. The peaks of chloroform at 369 and 263 cm<sup>-1</sup>, corresponding to the s-deformation and d-deformation transitions of C–Cl<sub>3</sub>, can be well-resolved. Remarkably, the intensity ratios of these peaks closely match the chemical concentration ratios with a detection sensitivity of 100 mM chloroform at this excitation power (Figures 2b and S3). Better sensitivity can be achieved with higher excitation power, especially with the pump laser. Utilizing the chloroform peak at 369 cm<sup>-1</sup>, we determine the spectral resolution of the hSRS system within the 200–400 cm<sup>-1</sup> range to be 12.8 cm<sup>-1</sup>

(Figure 2c). Alternatively, spectral fitting using the DMSO peaks yielded a similar resolution (Figure S4). In the C–H vibrational region, the spectral resolution was measured to be  $\sim 15$  cm<sup>-1</sup>. The spectral widths of the pump and Stokes pulses covered spectral windows of  $\sim 200$  cm<sup>-1</sup>.

In addition to analyzing low-scattering liquid samples, we applied the low-wavenumber hSRS microscope to investigate solid samples. Two chlorinated compounds, o,p'-DDT and TCHQ, are employed for the study. First, spontaneous Raman spectra of the chemicals, as depicted in Figures 3a,b, are acquired by using a lab-built confocal Raman system. The Raman shifts within the 200-400 cm<sup>-1</sup> range are magnified in enhanced detail. Subsequently, employing hSRS, we scan the same ranges and successfully detect Raman transitions with excellent spatial fidelity compared to that of the spontaneous Raman scattering spectra (Figure 3c,d). The two chemicals are then dissolved in chloroform and deposited onto a coverglass to allow solids to precipitate. Through hSRS imaging, we achieve the separation of different chemicals based on spectral distinctions (Figure 3e,f). Our observations reveal that in the drop-cast sample, DDT forms continuous spanning thin films, whereas TCHQ manifests as small globular structures. Such a morphological variation is likely caused by the solubility differences of the two substances in chloroform. DDT has a much higher solubility than TCHQ in chloroform. These results underscore how low-wavenumber SRS facilitates the detection of Raman transitions of chlorinated compounds by targeting the weaker vibrational energy.

Pushing the Detection Range below 200 cm<sup>-1</sup>. The hSRS spectral window spans approximately 200 cm<sup>-1</sup>. Switching between spectral windows requires adjusting the pump wavelength and slightly tuning the optical delay. The alteration in optical delay when transitioning from 1000 to 1035 nm is less than 0.5 mm. This wavelength change also affects the diffraction angle of the pump beam after it passes through the grating. Utilizing an 1800 lines/mm transmission grating, the angle change from 1015 to 1035 nm,

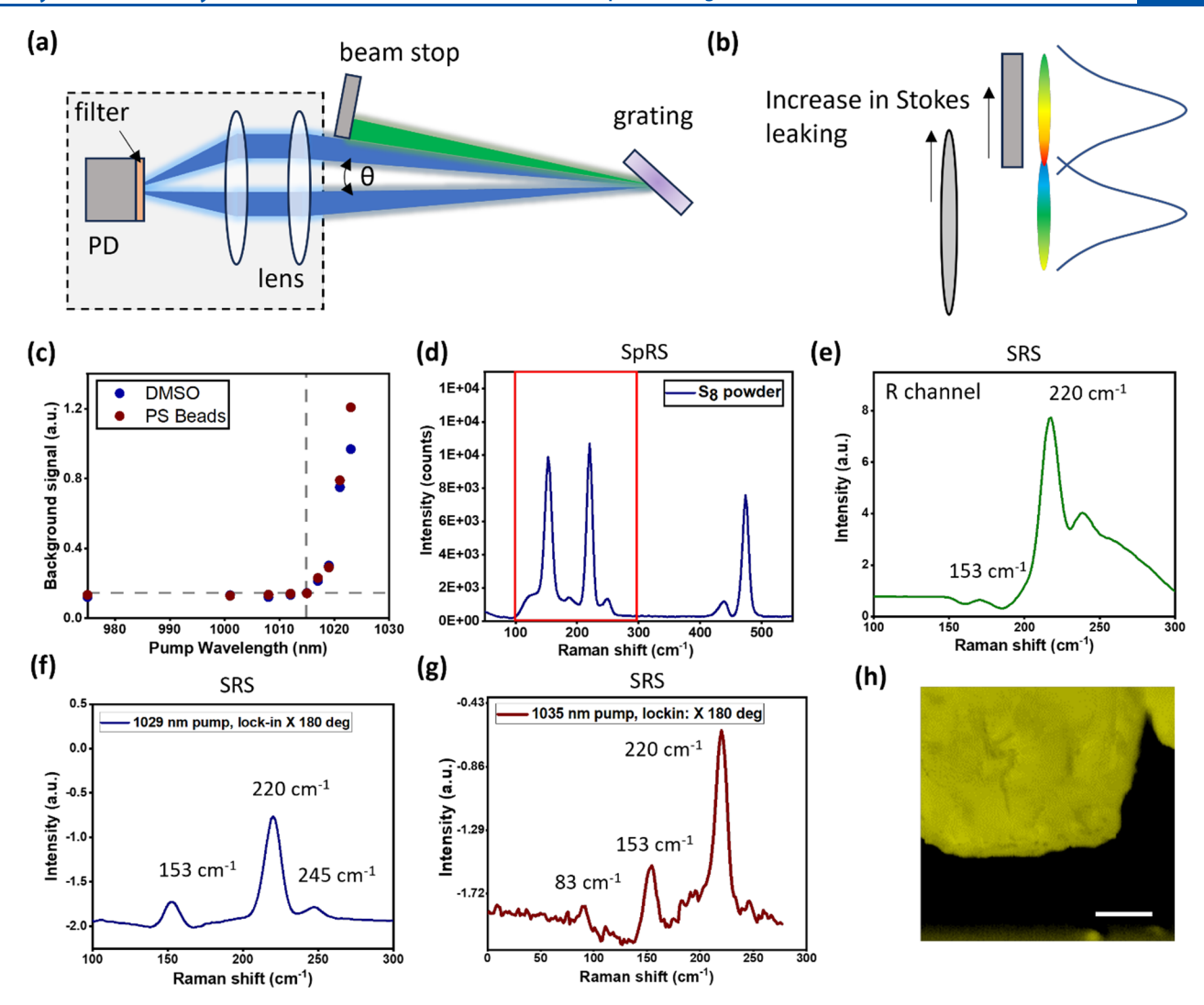


Figure 4. Detection of Raman shifts at lower wavenumbers. (a) Graphical representation of angle separation when tuning the pump excitation wavelength from 1015 to 1035 nm, with the beam spatial shift maintained within the lens diameter. (b) Illustration depicting the pump and Stokes beams at the beam stop and the first lens as the pump wavelength approaches the Stoke wavelength. The beam stop begins to obstruct the pump beam. As the beamstop and lens move in the direction of the arrow, the leakage of the Stokes beam into the detector increases. (c) SRS background at various pump wavelengths while maintaining the pump beam at the center of the collection lens. (d) Spontaneous Raman scattering (SpRS) spectrum of sulfur  $S_8$ . (e) hSRS spectrum of sulfur  $S_8$  detected using the lock-in R channel and a pump center wavelength of 1029 nm. (f) hSRS spectra of sulfur  $S_8$  obtained using the 180° lock-in phase in the X channel. (g) Sulfur  $S_8$  hSRS spectrum acquired using the 180° phase in the X channel at a pump wavelength of 1035 nm. (h) SRS image of sulfur film acquired at 153 cm<sup>-1</sup>. Scale bar: 20  $\mu$ m.

corresponding to the Raman transition from 282 to 92 cm<sup>-1</sup>, is 4.87°. A lens with a 150 mm focal length is employed to collimate the diffracted pump beam. The resulting 4.87° angle shift corresponds to a spatial beam shift of 12.7 mm on the lens (Figure 4a). Such a shift is smaller than the 25.4 mm lens diameter. Consequently, if only considering the lenses and detector, tuning the pump frequency from 1015 to 1035 nm does not necessitate realignment of the signal detection path.

However, at low wavenumbers, the beam stop can affect signal detection. As shown in Figure S1, the Stokes beam spectrum, which is centered at 1045 nm, exhibits a tail extending to below 1030 nm. When the pump beam wavelength is significantly shorter than this wavelength (e.g., center wavelength lower than 1017 cm<sup>-1</sup>), the Stokes beam can be efficiently separated and blocked without affecting the pump beam penetration. However, as the pump wavelength approaches 1030 nm, the beam stop begins to attenuate the frequency components of the pump, resulting in a reduction in

the SRS signals. Under this condition, adjusting the beam stop position and the detection components toward the longer wavelength, as illustrated in Figure 4a,b, can enhance pump beam detection but may simultaneously increase leakage of the Stokes beam into the detector. Additionally, even moving the collection lens toward the Stokes beam alone can increase the extent of Stokes beam leakage. Figure 4c illustrates the background signals when DMSO and polystyrene beads are used as samples while tuning the pump wavelengths and positioning the pump beam at the center of the lenses. Significant leakage of the Stokes beam occurs when the pump beam exceeds 1020 nm, corresponding to a wavelength of 234 cm<sup>-1</sup>. Furthermore, we also observed that stronger scattering from polystyrene beads contributes to greater leakage of the Stokes beam.

Hence, for optimal detection of Raman transitions below  $200~\text{cm}^{-1}$ , it is advisable not to use the R channel from the lock-in amplifier. We use sulfur  $S_8$  as an example to showcase

the enhancement of Raman signal detection and the suppression of Stokes beam leakage below 200 cm<sup>-1</sup> by phase-sensitive detection. In Figure 4d, the spontaneous Raman spectrum of sulfur is shown within the range 200-550 cm<sup>-1</sup>. Due to the limitation of the spectral filter, our labbuilt confocal spontaneous Raman system cannot detect Raman peaks lower than 100 cm<sup>-1</sup>. Figure 4e presents the SRS spectrum of sulfur acquired by tuning the pump wavelength to 1029 nm, corresponding to a center wavenumber of 149 cm<sup>-1</sup>. Applying the R channel of the lock-in amplifier, we could detect the symmetric S-S bending peak at 220 cm<sup>-1</sup> but not the asymmetric S-S bending peak at 153 cm<sup>-1</sup>.45 The negative signals observed at 153 cm<sup>-1</sup> result from interference of the SRS transition with the leaking Stokes beam, exhibiting opposite phases. In such instances, using a 180° phase shift in the lock-in X channel (Figure 4f) allows us to effectively separate the SRS signal from the Stokes beam leakage which has a 0° phase shift in the sample channel. This approach enables detection of the 153 cm<sup>-1</sup> transition from sulfur with a well-defined Lorentzian profile.

This phase-sensitive detection effectively mitigates the impact of Stokes beam leakage, whether caused by insufficient spatial blocking or sample scattering. The beam stop can even be removed when the pump beam is tuned to 1035 nm, corresponding to a central Raman shift of 92 cm<sup>-1</sup>. With this setup, we not only detect the signature peaks at 153 and 220 cm<sup>-1</sup> from sulfur but also resolve the low-wavenumber peak at 83 cm<sup>-1</sup> using hSRS. Moreover, the rejection of Stokes beam leakage enables the measurement of highly scattering samples. Figure 4h displays an image of a  $\sim$ 70  $\mu$ m thick sulfur film deposited on a glass slide, obtained using the 153 cm<sup>-1</sup> Raman peak. Using the current SRS system, we could not detect peaks below 83 cm<sup>-1</sup>. One possible reason is that the notch filter attenuates the pump wavelength components corresponding to these ultralow wavenumbers. Using the sulfur Raman peaks, we estimate the spectral resolution of the low-wavenumber SRS microscope to be  $\sim 11$  cm<sup>-1</sup> in the 120–280 cm<sup>-1</sup> region (Figure S5).

# CONCLUSIONS

We have demonstrated frequency-domain picosecond hSRS microscopy using spatial beam separation. This approach enables the measurement of Raman transitions below 400 cm<sup>-1</sup> with well-defined Lorentzian lineshapes. Moreover, the implementation of a phase-sensitive measurement allows the detection of Raman transitions below 100 cm<sup>-1</sup> and greatly mitigates the impact of sample scattering. Our hSRS system covers the spectral range from 100 to 4000 cm<sup>-1</sup> with a tunable spectral window of approximately 200 cm<sup>-1</sup>. This achievement is realized through simple modifications of a conventional hSRS microscope. We employ the spectral focusing method for acquiring SRS spectra, providing a spectral resolution from 11 to 16 cm<sup>-1</sup> in different spectral regions. Using this lowwavenumber hSRS microscope, we successfully measured Raman transitions of DMSO and several chlorinated molecules, including CHCl<sub>3</sub>, o,p'-DDT, and TCHQ. The hSRS microscopy technique allows for the spatial separation of o,p'-DDT and TCHO in drop-casted mixtures. Furthermore, we were able to detect sulfur Raman transitions as low as 83

Additional strategies can further enhance the sensitivity of the technology. For instance, employing a steeper filter with a cutoff frequency of around 1040 nm can reduce the leakage of Stokes pulses into the detector. Additionally, applying pulse shaping to create a sharp edge of the Stokes beam by eliminating lower wavelength components can further diminish the background induced by leakage. The hSRS system described in this study modulates the Stokes beam while detecting stimulated Raman loss. Transitioning the SRS configuration to modulate the pump beam while detecting the stimulated Raman gain could potentially simplify detection, as the detected beam would not change direction during wavelength tuning. Implementing these technological advancements would significantly modify the configuration of the existing hSRS microscope and thus will be explored in future research. Expanding the detection range to the lattice vibrational range would enhance SRS microscopy for studying material allotropy and changes in physical phases.

Extending the spectral coverage range to below 400 cm<sup>-1</sup> enables the detection of Raman transitions and chemicals that were previously undetectable by using conventional frequencydomain hSRS systems. This spectral range is important for imaging pharmaceutical ingredients such as chlorinated compounds which have strong Raman signatures in the lowwavenumber region. By avoiding crowded fingerprint regions and focusing on the low-wavenumber carbon—chlorine bonds, better detection of these compounds becomes possible. Lowwavenumber detection makes SRS possible to measure elements or compounds that only have Raman shifts in this region, such as sulfur, which are widely used in ointments and cosmetics. The low-wavenumber SRS imaging would also enable the mapping of various inorganic compounds such as calcium chloride and zinc selenide for material and environmental sciences.

## ASSOCIATED CONTENT

## Supporting Information

The Supporting Information is available free of charge at https://pubs.acs.org/doi/10.1021/acs.analchem.4c01298.

Spectra of Stokes and pump beams from the InSight X3+ femtosecond laser, optical density (OD) of the 1064 nm Notch filter, SRS signal-to-noise ratio (SNR) of CHCl<sub>3</sub>, SRS spectra of DMSO in the C–H and low-wavenumber regions, and SRS spectra of sulfur  $S_8$  in the 120–280 cm<sup>-1</sup> range (PDF)

# AUTHOR INFORMATION

# **Corresponding Author**

Chi Zhang — Department of Chemistry, Purdue University, West Lafayette, Indiana 47907, United States; Purdue Center for Cancer Research, West Lafayette, Indiana 47907, United States; Immunology, and Infectious Disease, Purdue Institute of Inflammation, Immunology and Infectious Disease, West Lafayette, Indiana 47907, United States; orcid.org/0000-0002-7735-5614; Email: zhan2017@purdue.edu

#### **Authors**

Matthew G. Clark — Department of Chemistry, Purdue University, West Lafayette, Indiana 47907, United States Karsten J. Mohn — Department of Chemistry, Purdue University, West Lafayette, Indiana 47907, United States; orcid.org/0009-0005-3097-9322

Bin Dong – Department of Chemistry, Purdue University, West Lafayette, Indiana 47907, United States; Purdue Center

for Cancer Research, West Lafayette, Indiana 47907, United States; orcid.org/0000-0003-4741-3593

Helen C. Campbell – Department of Chemistry, Purdue University, West Lafayette, Indiana 47907, United States

Complete contact information is available at: https://pubs.acs.org/10.1021/acs.analchem.4c01298

## **Author Contributions**

M.G.C., K.J.M., and C.Z. performed the experiments. M.G.C. analyzed the results. K.J.M. and H.C. were involved in the data acquisition. B.D. assisted in developing the imaging software. C.Z. developed the idea, obtained the funding, and supervised the work. All authors have approved the final version of the manuscript.

## **Notes**

The authors declare no competing financial interest.

## ACKNOWLEDGMENTS

The authors acknowledge Shivam Mahapatra for his help in preparing the sulfur sample and Gregory Eakins for the design and fabrication of the resonant amplifier used in the photodiode. We acknowledge Chloe Zhang for her assistance in designing the cover art. This work is supported by the Center for Bioanalytic Metrology grant (an NSF Industry-University Cooperative Research Center under NSF IIP 1916991, C.Z.) and the NIH R35GM147092.

# REFERENCES

- (1) Zumbusch, A.; Holtom, G. R.; Xie, X. S. Phys. Rev. Lett. 1999, 82 (20), 4142.
- (2) Cheng, J.-X.; Volkmer, A.; Xie, X. S. J. Opt. Soc. Am. B **2002**, 19 (6), 1363–1375.
- (3) Freudiger, C. W.; Min, W.; Saar, B. G.; Lu, S.; Holtom, G. R.; He, C.; Tsai, J. C.; Kang, J. X.; Xie, X. S. Science **2008**, 322 (5909), 1857–1861.
- (4) Ozeki, Y.; Dake, F.; Kajiyama, S. I.; Fukui, K.; Itoh, K. Opt. Express 2009, 17 (5), 3651-3658.
- (5) Nandakumar, P.; Kovalev, A.; Volkmer, A. New J. Phys. 2009, 11 (3), No. 033026.
- (6) Min, W.; Freudiger, C. W.; Lu, S.; Xie, X. S. Annu. Rev. Phys. Chem. 2011, 62, 507-530.
- (7) Suhalim, J. L.; Boik, J. C.; Tromberg, B. J.; Potma, E. O. J. *Biophotonics* **2012**, 5 (5–6), 387–395.
- (8) Camp, C. H., Jr; Lee, Y. J.; Heddleston, J. M.; Hartshorn, C. M.; Walker, A. R. H.; Rich, J. N.; Lathia, J. D.; Cicerone, M. T. *Nat. Photonics* **2014**, *8* (8), 627–634.
- (9) Zhang, C.; Zhang, D.; Cheng, J.-X. Annu. Rev. Biomed. Eng. 2015, 17, 415-445.
- (10) Polli, D.; Kumar, V.; Valensise, C. M.; Marangoni, M.; Cerullo, G. Laser Photonics Rev. 2018, 12 (9), No. 1800020.
- (11) Manifold, B.; Fu, D. Annu. Rev. Anal. Chem. 2022, 15, 269-289.
- (12) Cheng, J.-X.; Xie, X. S. Science 2015, 350 (6264), No. aaa8870.
- (13) Zhang, D.; Wang, P.; Slipchenko, M. N.; Ben-Amotz, D.; Weiner, A. M.; Cheng, J.-X. Anal. Chem. 2013, 85 (1), 98-106.
- (14) Fu, D.; Holtom, G.; Freudiger, C.; Zhang, X.; Xie, X. S. J. Phys. Chem. B 2013, 117 (16), 4634–4640.
- (15) Wang, P.; Li, J.; Wang, P.; Hu, C. R.; Zhang, D.; Sturek, M.; Cheng, J. X. Angew. Chem. Int. Ed. 2013, 125 (49), 13280–13284.
- (16) Yan, Y. X.; Nelson, K. A. J. Chem. Phys. 1987, 87 (11), 6257–6265.
- (17) Ruhman, S.; Joly, A. G.; Nelson, K. A. IEEE J. Quantum Electron. 1988, 24 (2), 460-469.

- (18) Raanan, D.; Audier, X.; Shivkumar, S.; Asher, M.; Menahem, M.; Yaffe, O.; Forget, N.; Rigneault, H.; Oron, D. *Opt. Lett.* **2019**, 44 (21), 5153–5156.
- (19) Shivkumar, S.; Ranann, D.; Metais, S.; Suresh, S.; Forget, N.; Bartels, R.; Oron, D.; Rigneault, H. *Phys. Rev. Appl.* **2023**, *19* (5), No. 054075.
- (20) Liao, C.-S.; Cheng, J.-X. Annu. Rev. Anal. Chem. 2016, 9, 69–93.
- (21) Hu, F.; Shi, L.; Min, W. Nat. Methods 2019, 16 (9), 830-842.
- (22) Zhang, C.; Aldana-Mendoza, J. A. JPhys. Photonics 2021, 3 (3), No. 032002.
- (23) Li, Y.; Shen, B.; Li, S.; Zhao, Y.; Qu, J.; Liu, L. Adv. Biol. 2021, 5 (1), No. e2000184.
- (24) Koike, K.; Smith, N. I.; Fujita, K. Biomed Opt. Express 2022, 13 (2), 995-1004.
- (25) Ji, M.; Orringer, D. A.; Freudiger, C. W.; Ramkissoon, S.; Liu, X.; Lau, D.; Golby, A. J.; Norton, I.; Hayashi, M.; Agar, N. Y.; Young, G. S.; Spino, C.; Santagata, S.; Camelo-Piragua, S.; Ligon, K. L.; Sagher, O.; Xie, X. S. Sci. Transl. Med. 2013, 5 (201), 201ra119 DOI: 10.1126/scitranslmed.3005954.
- (26) Liao, C.-S.; Slipchenko, M. N.; Wang, P.; Li, J.; Lee, S.-Y.; Oglesbee, R. A.; Cheng, J.-X. *Light Sci. Appl.* **2015**, 4 (3), e265.
- (27) Liao, C.-S.; Wang, P.; Wang, P.; Li, J.; Lee, H. J.; Eakins, G.; Cheng, J.-X. Sci. Adv. 2015, 1 (9), No. e1500738.
- (28) Li, J.; Condello, S.; Thomes-Pepin, J.; Ma, X.; Xia, Y.; Hurley, T. D.; Matei, D.; Cheng, J.-X. Cell Stem Cell **2017**, 20 (3), 303–314. e5
- (29) Wei, L.; Yu, Y.; Shen, Y.; Wang, M. C.; Min, W. Proc. Natl. Acad. Sci. U. S. A. 2013, 110 (28), 11226–11231.
- (30) Fu, D.; Yu, Y.; Folick, A.; Currie, E.; Farese, R. V., Jr; Tsai, T.-H.; Xie, X. S.; Wang, M. C. J. Am. Chem. Soc. **2014**, 136 (24), 8820–8828
- (31) Wei, L.; Hu, F.; Chen, Z.; Shen, Y.; Zhang, L.; Min, W. Acc. Chem. Res. **2016**, 49 (8), 1494–1502.
- (32) Bae, K.; Zheng, W.; Ma, Y.; Huang, Z. Theranostics 2019, 9 (5), 1348.
- (33) Zhang, M.; Hong, W.; Abutaleb, N. S.; Li, J.; Dong, P. T.; Zong, C.; Wang, P.; Seleem, M. N.; Cheng, J. X. Adv. Sci. 2020, 7 (19), No. 2001452.
- (34) Chen, C.; Wang, Y.; Wu, F.; Hong, W. Anal. Chem. 2023, 95 (42), 15556–15565.
- (35) Wang, P.; Liu, B.; Zhang, D.; Belew, M. Y.; Tissenbaum, H. A.; Cheng, J. X. Angew. Chem. **2014**, 126 (44), 11981–11986.
- (36) Fu, D.; Zhou, J.; Zhu, W. S.; Manley, P. W.; Wang, Y. K.; Hood, T.; Wylie, A.; Xie, X. S. *Nat. Chem.* **2014**, *6* (7), 614–622.
- (37) Liu, B.; Wang, P.; Kim, J. I.; Zhang, D.; Xia, Y.; Chapple, C.; Cheng, J.-X. Anal. Chem. **2015**, 87 (18), 9436–9442.
- (38) Shen, W.; Collings, C.; Li, M.; Markovicz, J.; Ralph, J.; Mansfield, S. D.; Ding, S.-Y. ACS Sustain. Chem. Eng. 2019, 7 (12), 10616–10622.
- (39) Laptenok, S. P.; Rajamanickam, V. P.; Genchi, L.; Monfort, T.; Lee, Y.; Patel, I. I.; Bertoncini, A.; Liberale, C. *J. Biophotonics* **2019**, *12* (9), No. e201900028.
- (40) Lin, H.; Lee, H. J.; Tague, N.; Lugagne, J.-B.; Zong, C.; Deng, F.; Wong, W.; Dunlop, M. J.; Cheng, J.-X. Nat. Commun. 2020, 12, 8688.
- (41) Clark, M. G.; Brasseale, K. A., III; Gonzalez, G. A.; Eakins, G.; Zhang, C. J. Vis. Exp. **2022**, 182, No. e63677.
- (42) Clark, M. G.; Gonzalez, G. A.; Zhang, C. Anal. Chem. 2022, 94 (44), 15405–15414.
- (43) Clark, M. G.; Gonzalez, G. A.; Luo, Y.; Aldana-Mendoza, J. A.; Carlsen, M. S.; Eakins, G.; Dai, M.; Zhang, C. *Nat. Commun.* **2022**, *13* (1), 4343.
- (44) Martens, W. N.; Frost, R. L.; Kristof, J.; Theo Kloprogge, J. J. Raman Spectrosc. **2002**, 33 (2), 84–91.
- (45) Nims, C.; Cron, B.; Wetherington, M.; Macalady, J.; Cosmidis, J. Sci. Rep. **2019**, 9 (1), 7971.